

See discussions, stats, and author profiles for this publication at: <https://www.researchgate.net/publication/242331987>

# Corrosion/Fragmentation of Layered Composite Cathode and Related Capacity/Voltage Fading during Cycling Process

ARTICLE *in* NANO LETTERS · JUNE 2013

Impact Factor: 13.59 · DOI: 10.1021/nl401849t · Source: PubMed

---

CITATIONS

71

---

READS

111

6 AUTHORS, INCLUDING:



Jianming Zheng

Pacific Northwest National Laboratory

62 PUBLICATIONS 1,488 CITATIONS

SEE PROFILE



Meng Gu

University of California, Davis

69 PUBLICATIONS 1,318 CITATIONS

SEE PROFILE

# Corrosion/Fragmentation of Layered Composite Cathode and Related Capacity/Voltage Fading during Cycling Process

Jianming Zheng,<sup>†</sup> Meng Gu,<sup>‡</sup> Jie Xiao,<sup>†</sup> Pengjian Zuo,<sup>†</sup> Chongmin Wang,<sup>\*,‡</sup> and Ji-Guang Zhang<sup>\*,†</sup>

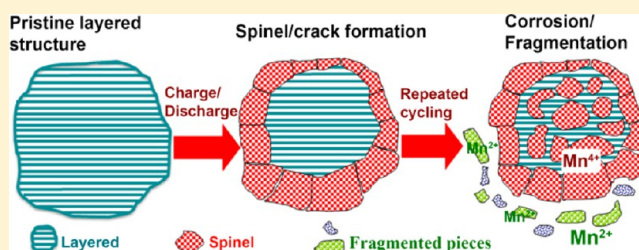
<sup>†</sup>Energy and Environmental Directorate and <sup>‡</sup>Environmental Molecular Sciences Laboratory, Pacific Northwest National Laboratory, Richland, Washington 99352, United States

## S Supporting Information

**ABSTRACT:** The Li-rich, Mn-rich (LMR) layered structure materials exhibit very high discharge capacities exceeding 250 mAh g<sup>-1</sup> and are very promising cathodes to be used in lithium ion batteries. However, significant barriers, such as voltage fade and low rate capability, still need to be overcome before the practical applications of these materials. A detailed study of the voltage/capacity fading mechanism will be beneficial for further tailoring the electrode structure and thus improving the electrochemical performances of these layered cathodes.

Here, we report detailed studies of structural changes of LMR layered cathode Li[Li<sub>0.2</sub>Ni<sub>0.2</sub>Mn<sub>0.6</sub>]O<sub>2</sub> after long-term cycling by aberration-corrected scanning transmission electron microscopy (STEM) and electron energy loss spectroscopy (EELS). The fundamental findings provide new insights into capacity/voltage fading mechanism of Li[Li<sub>0.2</sub>Ni<sub>0.2</sub>Mn<sub>0.6</sub>]O<sub>2</sub>. Sponge-like structure and fragmented pieces were found on the surface of cathode after extended cycling. Formation of Mn<sup>2+</sup> species and reduced Li content in the fragments leads to the significant capacity loss during cycling. These results also imply the functional mechanism of surface coatings, for example, AlF<sub>3</sub>, which can protect the electrode from etching by acidic species in the electrolyte, suppress cathode corrosion/fragmentation, and thus improve long-term cycling stability.

**KEYWORDS:** Voltage fading, fragmentation, etched surface, Mn<sup>2+</sup> formation, layered cathode, lithium ion battery



Lithium ion batteries are one of the most promising energy storage technologies for electric vehicle (EV) and plug-in hybrid electric vehicle (PHEV) applications. The energy density and power density of LiCoO<sub>2</sub> cathode are among the best reported of various commercially available cathodes. However, LiCoO<sub>2</sub> is not suitable for large-scale EV/PHEV applications due to its high cost and poor availability. The search for high-capacity and safe cathode materials to replace LiCoO<sub>2</sub> has become one of the most important subjects in the study of cathode materials for high-energy-density Li-ion batteries. The layered-structure cathodes developed by Thackeray et al.<sup>1,2</sup> are composites of Li<sub>2</sub>MO<sub>3</sub> (C2/m) and LiMO<sub>2</sub> (R3m) (also called Li-rich, Mn-rich cathodes, or LMR) and can be expressed as  $x\text{Li}_2\text{MO}_3 \cdot (1-x)\text{LiMO}_2$  (M = Ni, Co, Mn, or combinations). The typical compositions of these cathodes include Li[Li<sub>0.2</sub>Ni<sub>0.2</sub>Mn<sub>0.6</sub>]O<sub>2</sub> (LMNO) and Li[Li<sub>0.2</sub>Mn<sub>0.54</sub>Ni<sub>0.13</sub>Co<sub>0.13</sub>]O<sub>2</sub>, both of which can deliver much higher capacity with a significant cost reduction compared to traditional cathode materials such as LiCoO<sub>2</sub> and LiMn<sub>2</sub>O<sub>4</sub> spinel.<sup>1,2</sup> The Li<sub>2</sub>MO<sub>3</sub> component can stabilize the electrode structure and enhance the discharge capacity of the electrode by extracting the lithium ions concomitant with release of oxygen (a net loss of Li<sub>2</sub>O), typically at 4.4–4.6 V.<sup>3</sup> After activation of the Li<sub>2</sub>MO<sub>3</sub> component in the initial charge process, a discharge capacity of higher than 250 mAh g<sup>-1</sup> can be achieved for these layered-structure cathodes. If activated at an elevated temperature of 50 °C, an even higher discharge capacity (>300 mAh g<sup>-1</sup>) could be obtained.<sup>4</sup> Because of their attractive

properties, researchers all over the world have put forth much effort in investigating these Li-rich, Mn-rich layered materials as cathodes for Li-ion batteries.<sup>5</sup> However, significant challenges, including voltage decay, long-term cycling instability, and poor rate capability, have to be overcome prior to the practical application of these layered composite cathodes.

It is well-known that the extensive removal of Li<sup>+</sup> ions leads to instability of the electrode structure, resulting in the structural transformation from the layered to spinel phase. This phase transformation has been proposed and considered as one primary factor contributing to the voltage instability, capacity fading, and poor rate performance of the layered composite cathodes.<sup>6–9</sup> It is well-accepted that the formation of spinel phase leads to the appearance of a ~3.0 V plateau, which is responsible for the voltage decay of the electrode. However, lithium ion insertion into/extraction out of the spinel phase still occurs within the preset voltage range (e.g., 2.0–4.8 V), even though the lithium ion transport appears to be slower in the transformed spinel phase than in the layered phase.<sup>10</sup> Furthermore, it is not well-understood whether the transformed spinel phase is stable or how the capacity decays during subsequent cycling. A more detailed atomic scale structural and chemical analysis on the cycled electrode will help answer these questions.

**Received:** May 21, 2013

**Revised:** June 25, 2013

**Published:** June 26, 2013

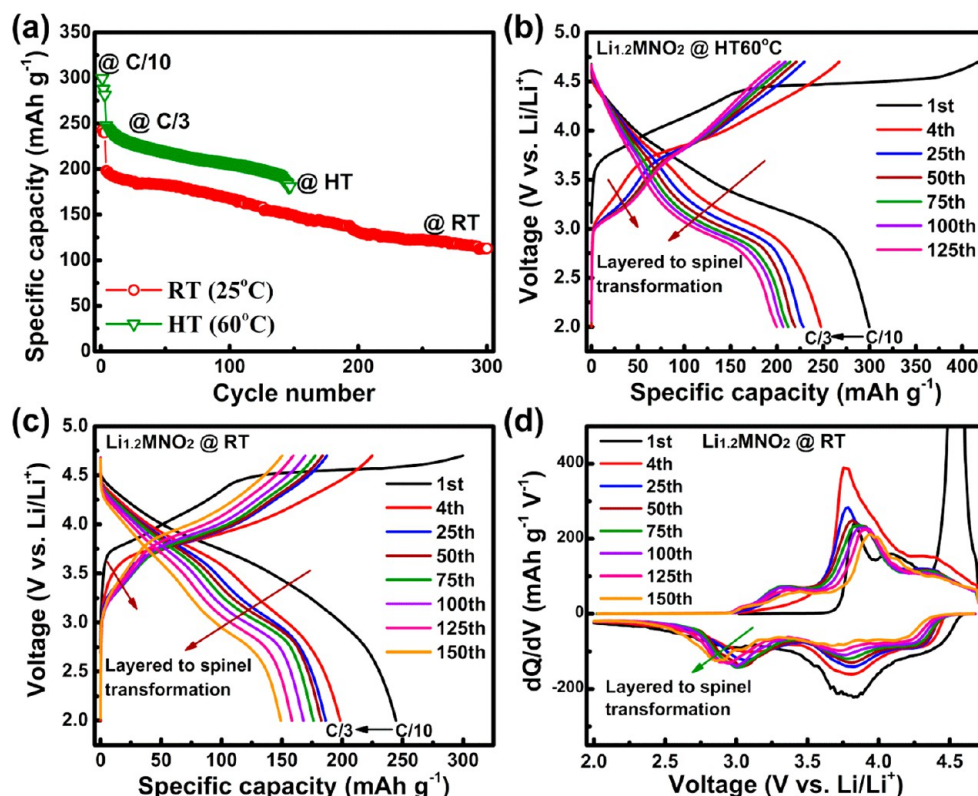


**Figure 1.** (a) Cycling performance; (b and c) charge/discharge profiles at RT ( $\sim 25^\circ\text{C}$ ) and HT ( $60^\circ\text{C}$ ); (d)  $dQ/dV$  curves at RT of cathode material  $\text{Li}[\text{Li}_{0.2}\text{Ni}_{0.2}\text{Mn}_{0.6}]\text{O}_2$ .

Here, we used aberration-corrected scanning transmission electron microscopy (STEM) combined with electron energy loss spectroscopy (EELS) to probe the atomic structure of layered cathode  $\text{Li}[\text{Li}_{0.2}\text{Ni}_{0.2}\text{Mn}_{0.6}]\text{O}_2$  (LNMO) before and after long-term high voltage cycling. The atomic contrast in high-angle annular dark field (HAADF) STEM imaging could identify the changes in stacking and ordering in the cycled particles, while EELS chemical analysis could reveal important chemistry changes. Based on the results of STEM observations and the EELS characterization, a more detailed understanding of the capacity fading mechanism of LNMO beyond spinel transformation during long-term cycling was obtained.

Electrochemical performances of cathode material  $\text{Li}[\text{Li}_{0.2}\text{Ni}_{0.2}\text{Mn}_{0.6}]\text{O}_2$  were investigated in coin cells using  $\text{Li}_4\text{Ti}_5\text{O}_{12}$  (LTO) or metallic lithium foil as the negative electrode. The LNMO/LTO cell exhibits relatively faster capacity degradation than LNMO/Li cell (see Figure S1 in the Supporting Information). This result can be attributed to the imbalance of Coulombic efficiency between LTO and LNMO cathode as well as the capacity/voltage fading of LNMO cathode. In contrast, using metallic lithium foil as anode could provide a large excess of lithium source and stable potential, which enables us to focus on study of the capacity/voltage fading mechanism of lithium-rich layered cathode material  $\text{Li}[\text{Li}_{0.2}\text{Ni}_{0.2}\text{Mn}_{0.6}]\text{O}_2$ . Cycling performance together with corresponding charge/discharge profile and differential capacity-versus-voltage ( $dQ/dV$ ) curve evolutions of cathode material  $\text{Li}[\text{Li}_{0.2}\text{Ni}_{0.2}\text{Mn}_{0.6}]\text{O}_2$  are shown in Figure 1a–d. During formation cycles at C/10, the electrode material could deliver a capacity of ca.  $250\text{ mAh g}^{-1}$ . After three formation cycles, with the current density increased to C/3,  $198\text{ mAh g}^{-1}$  of capacity still could be achieved. The  $\text{Li}[\text{Li}_{0.2}\text{Ni}_{0.2}\text{Mn}_{0.6}]\text{O}_2$  material shows gradual capacity decay both

at room temperature (RT) ( $\sim 25^\circ\text{C}$ ) and high temperature (HT) of  $60^\circ\text{C}$  (in spite of its high capacity), which could be ascribed to the deteriorated electrode/electrolyte interface that hampers the reversible lithium ion intercalation/deintercalation.<sup>11–13</sup> After 300 cycles at RT, the electrode shows a discharge capacity of only  $113\text{ mAh g}^{-1}$ , with a low capacity retention of 57.1%. The detailed voltage/capacity curves of the  $\text{Li}[\text{Li}_{0.2}\text{Ni}_{0.2}\text{Mn}_{0.6}]\text{O}_2$  cathode are presented in Figure 1b and c.

These results clearly show that the initial charge profile is accompanied by an irreversible voltage plateau at 4.4–4.6 V for oxidation beyond the formal oxidation potential of  $\text{Ni}^{2+}$  to  $\text{Ni}^{3+}$  and then to  $\text{Ni}^{4+}$ . The voltage plateaus have been assigned to an irreversible loss of oxygen from the structural lattice based on in situ X-ray diffraction studies<sup>14</sup> and differential electrochemical mass spectrometry (DEMS) results.<sup>11,15</sup> During the oxygen loss plateau, the  $\text{Li}_2\text{MO}_3$  component is activated, and thus the material could deliver high discharge capacity during the subsequent discharge process. However, to achieve a high discharge capacity, the electrode has to be charged to high cutoff voltage of ca. 4.6–4.8 V, to activate the  $\text{Li}_2\text{MnO}_3$  component. The extensive removal of lithium ions and the concomitant oxygen evolution result in the instability of the electrode structure and lead to a phase transformation from layered to spinel and/or even lattice breakdown.<sup>6,8</sup> Direct evidence for layered/spinel transformation has been observed with STEM by Gu et al.<sup>9</sup> and Xu et al.<sup>8</sup> The structural transformation leads to a layered-spinel intergrown structure and the evolution of a redox reaction in the ca. 3.0 V region, as observed from Figure 1b and c, which is consistent with that reported for  $0.7\text{ Li}_2\text{MnO}_3 \cdot 0.3\text{ LiNi}_{1/3}\text{Co}_{1/3}\text{Mn}_{1/3}\text{O}_2$ .<sup>6</sup> The discharge profile shows obvious voltage decay with the increasing cycle number. The midpoint voltage (MPV) of discharge decreases from 3.57 V at the fourth



cycle to 3.38 V at the 100th cycle when cycled at RT; when cycled at 60 °C, it changes from 3.28 V at the fourth cycle to 3.10 V at the 100th cycle. Figure 1d presents the  $dQ/dV$  curve evolutions of the  $\text{Li}[\text{Li}_{0.2}\text{Ni}_{0.2}\text{Mn}_{0.6}]\text{O}_2$  electrode during cycling at RT. The electrode shows a gradual increase of intercalation peak intensity at ca. 3.0 V, due to the increasing formation of spinel phase within the electrode structure.

In principle, layered/spinel transformation involves migration of transition metal (TM) ions into Li sites and Li ions into the tetrahedral sites followed by a distortion of oxygen lattices.<sup>7</sup> Clear evidence for the formation of spinel-like phase on the electrode surface has been reported for  $\text{Li}[\text{Li}_{0.2}\text{Ni}_{0.2}\text{Mn}_{0.6}]\text{O}_2$  material after high voltage cycling.<sup>8</sup> As reported, with the extensive removal of lithium ions at high voltage, the migration of the TM ions into the Li layer is energetically favorable in the high voltage region and thus could facilitate the formation of spinel-like phase. A few unit cells of spinel phase is observed to form on the surface area after 10 cycles.<sup>8</sup> More recently, prolonged charge/discharge cycling (300 cycles) has also been demonstrated to extend the  $\text{LiMn}_2\text{O}_4$ -type spinel formation from the surface region to the interior of the particles.<sup>9</sup> The layered/spinel phase transformation is considered as one of the primary factors responsible for the voltage decay, capacity fading, and poor rate performance of layered-structure electrodes with  $\text{Li}_2\text{MnO}_3$ -like character. The voltage decay of the battery upon cycling can be directly correlated with the layered/spinel transformation. However, the layered/spinel transformation could not exclusively explain the continuous capacity fading because significantly improved cycling stability could be achieved in  $\text{AlF}_3$ -coated material even though the layered/spinel phase transformation still occurs, as evidenced by the obvious evolution of the 3 V plateau.<sup>9,11</sup> It is speculated that the capacity fading is associated with the further degradation of spinel phase converted from the layered structure. This is possible because, if fully activated at high potentials (378  $\text{mAh g}^{-1}$ ) and discharged back to the rock salt stoichiometry,  $\text{LiNi}_{0.25}\text{Mn}_{0.75}\text{O}_2$  (282  $\text{mAh g}^{-1}$ ), the average oxidation state of manganese in the discharged electrode is only 3.33, which is below the manganese oxidation state of 3.5 and expected for a potentially damaging Jahn–Teller distortion. Therefore, it is still not clear how the spinel phase evolves in the layered cathode material  $\text{Li}[\text{Li}_{0.2}\text{Ni}_{0.2}\text{Mn}_{0.6}]\text{O}_2$  during extended cycling of the battery. In the following section, we report the details of the structural evolution of the spinel phase with the progression of the repeated charge/discharge of the battery.

The microstructure of the pristine material is illustrated in Figure 2a, demonstrating that the material before electrochemical charge/discharge processes is composed of well-crystallized particles. The overview Z-contrast image in Figure 2b shows that the pristine  $\text{Li}[\text{Li}_{0.2}\text{Ni}_{0.2}\text{Mn}_{0.6}]\text{O}_2$  cathode exhibits well-defined layered structure, with a stacking sequence of Li/O/TM/O. The layered  $\text{Li}[\text{Li}_{0.2}\text{Ni}_{0.2}\text{Mn}_{0.6}]\text{O}_2$  is a composite of the intergrowth of  $\text{LiMO}_2$  ( $R\bar{3}m$ ) and  $\text{Li}_2\text{MnO}_3$  ( $C2/m$ ) phases distributed at the nanoscale.<sup>9,16</sup> The atomic resolution image together with the atomic model, as shown in Figure 2c, belongs to the  $[010]$  zone projection of the layered structure. The lithium ion row corresponds to the least intensity in comparison with the O sites and the brightest TM sites. A simulated Z-contrast image, showing that the TM layer exhibits the highest intensity while the Li layer is almost invisible, is also provided in Figure 2d for comparison. Such a pattern of one brighter column followed by a very dark column clearly reveals that the replacement of Li ions by TM ions in the Li layer is less than 10%.<sup>16</sup> These observations

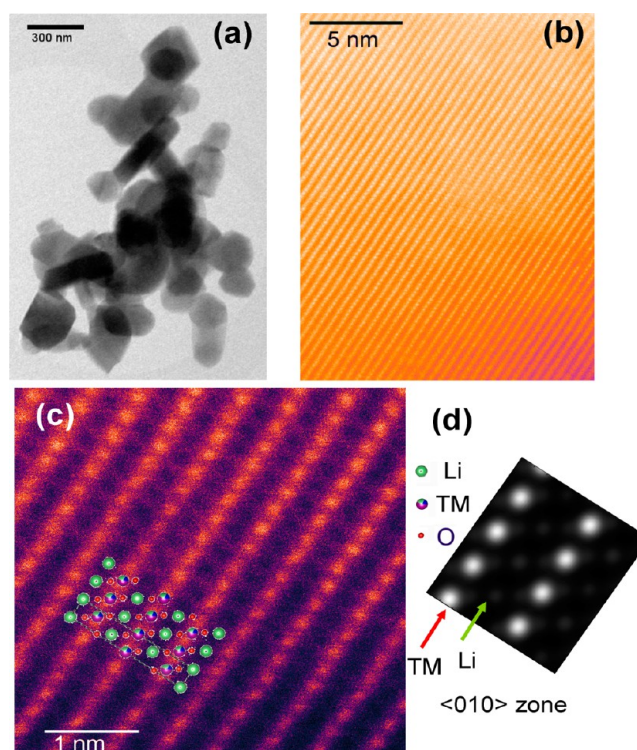


**Figure 2.** (a) High-resolution transmission electron microscopy image and (b) overview Z-contrast image of the pristine  $\text{Li}[\text{Li}_{0.2}\text{Ni}_{0.2}\text{Mn}_{0.6}]\text{O}_2$  cathode; (c) atomic resolution image; (d) simulated Z-contrast image of the  $[010]$  projection with 10% Li/Ni disorder.

are quite consistent with the results reported by Gu et al.<sup>9</sup> and Xu et al.<sup>8</sup>

After 300 cycles, two obvious features can be seen from the microstructures of the particles. First, microcracks could be clearly observed in the cycled particles as indicated with white arrows in the STEM image in Figure 3a. Similar observations of crack formation have been reported by other researchers for  $\text{Li}_2\text{MO}_3$ -containing layered cathode material, which is believed to originate from the large strain generated by extensive removal of lithium ions concomitant with extraction of oxygen (net loss of “ $\text{Li}_2\text{O}$ ”) during charging.<sup>9,17,18</sup> This detrimental effect obviously leads to the loss of contact between different regions even within the same particle, which dramatically hampers the lithium ion diffusion and electron transport within the material particles. The end result is the rapid increase of cell resistance (Figure 3b) and continuous degradation of reversible capacity during extended cycling, especially at high current rates. The percentage of crack formation in the nanoparticles is only a few percent based on the electron microscopy images of more than 300 particles. We believe that the crack formation is size-dependent. As reported by Miller et al., similar crack formation is more common in micrometer-sized layered cathode materials as confirmed by their in situ SEM results.<sup>19</sup> In addition, pristine material exhibits single-crystalline quality as shown by the STEM image (Figure S2a in the Supporting Information) and the corresponding fast Fourier transform (FFT) pattern (Figure S2b). In contrast, the polycrystalline nature of the cycled samples can be clearly observed from the STEM images shown in Figure S2c and the corresponding FFT pattern shown in Figure S2d. The results reveal that, after repeated cycling, the nanoparticles partially changes to polycrystalline with structural defects and amorphous regions.

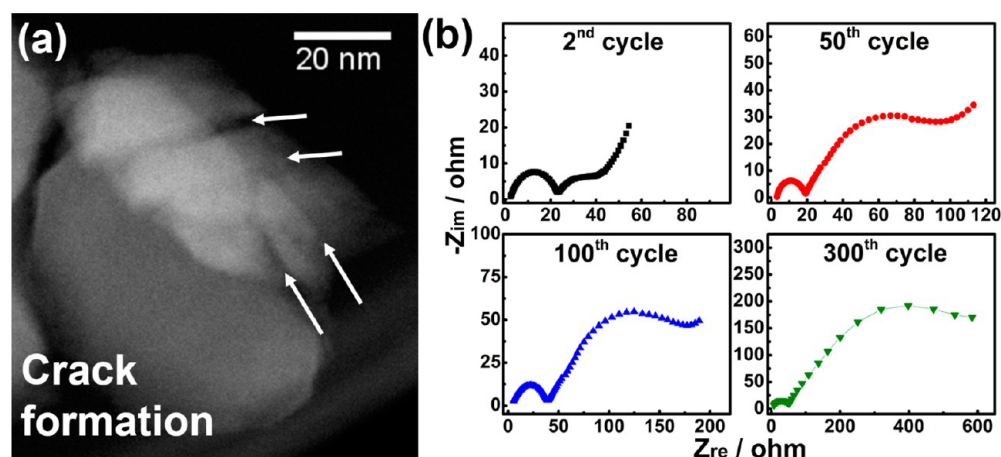


**Figure 3.** (a) STEM image showing the formation of microcracks in LNMO after 300 cycles; (b) EIS spectra evolution during cycling to 300 cycles.

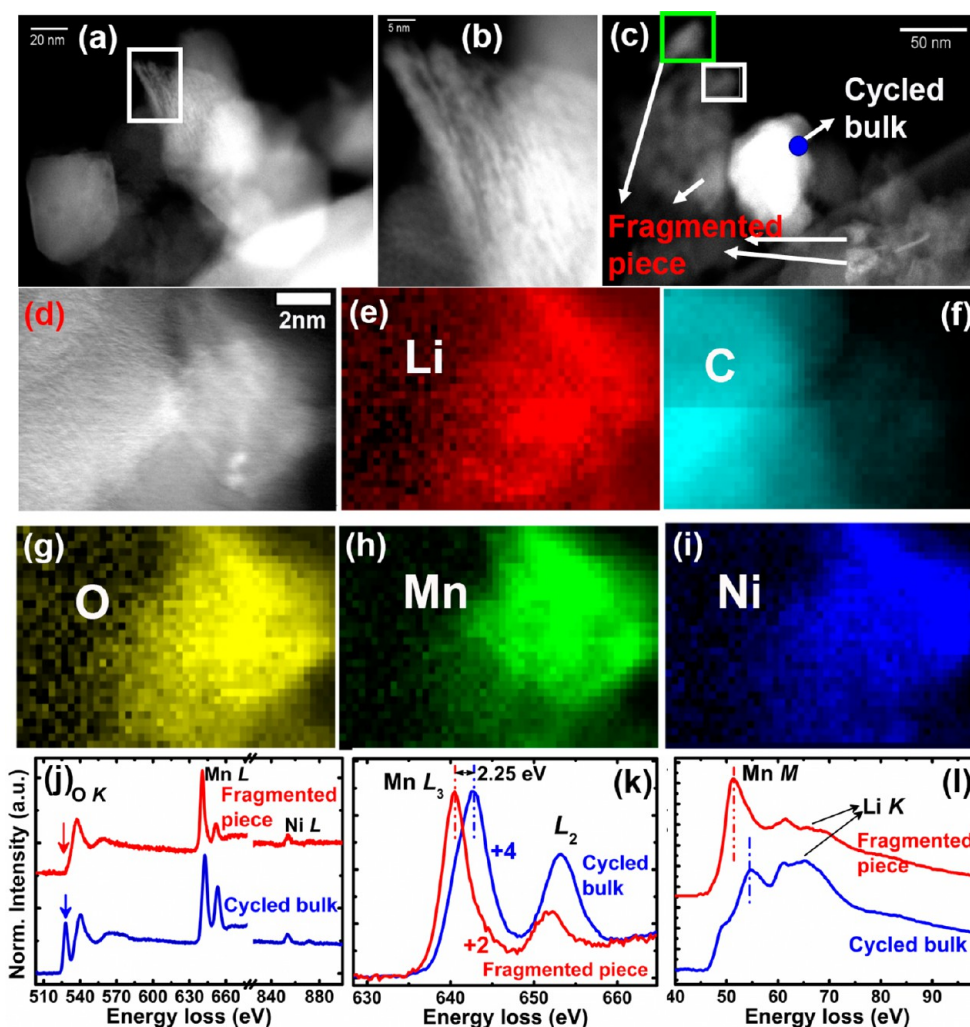


**Figure 4.** (a) Overview image showing the cathode nanoparticles after cycling; (b) magnified image of the region labeled by the white rectangle shown in a; (c) overview image of another region with fragmented pieces of cathode; (d) magnified image of the region labeled by white rectangle in c; (e) Li map (58.25–65.5 eV); (f) C map (282.25–314.75 eV); (g) O map (527.75–564 eV); (h) Mn map (634.25–659 eV); (i) Ni map (850.25–858.5 eV); (j) comparison of O K, Mn L, and Ni L edges; (k) Mn L edge comparison normalized to Mn  $L_3$  peak; (l) Mn M and Li K edge comparison of cycled bulk region and fragmented piece region.

In addition to the microcracks, sponge-like etched surface regions without fringe contrast could be clearly observed in the cycled particles, as shown in Figure 4a and b, which is in good agreement with other reports for similar layered composite

cathodes.<sup>19,17</sup> This kind of etched surface is unfavorable for lithium ion insertion/extraction and could be a serious cause of cyclic deterioration. Parts of the severely etched surface would separate from the bulk and become fragmented pieces. As



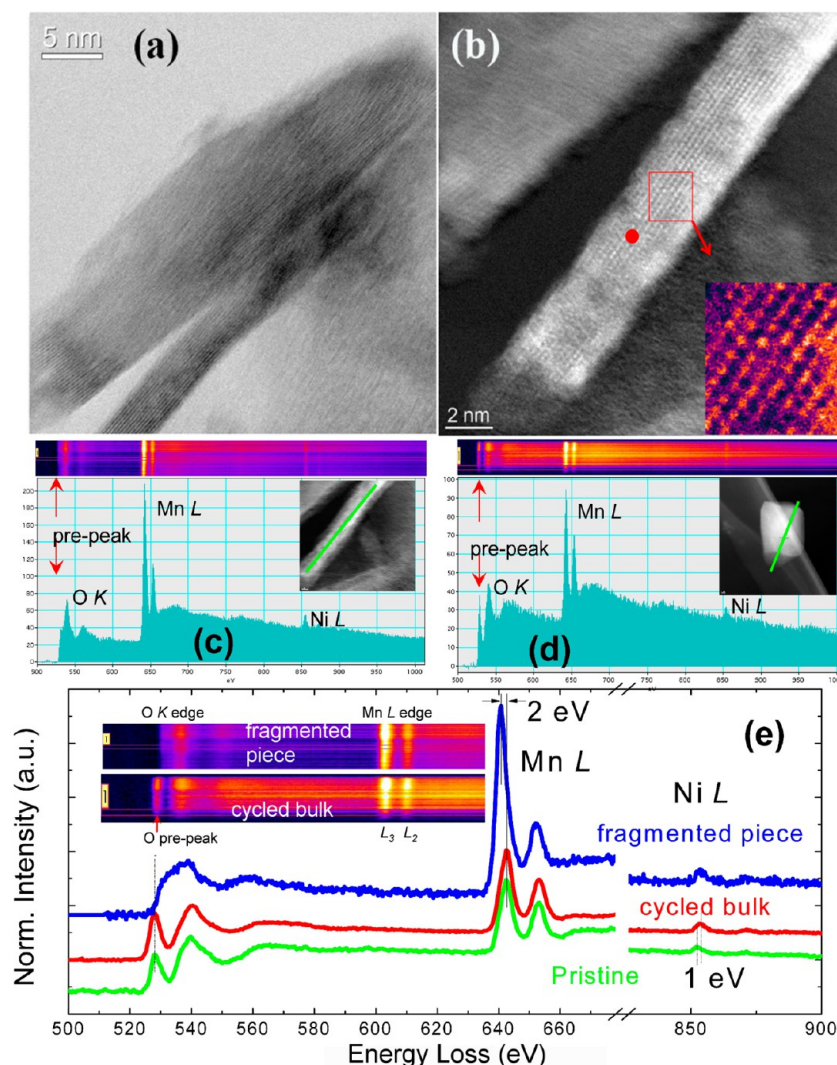


**Figure 5.** (a) Bright field image showing lattice fringes in this region. (b) Z-contrast image showing the destroyed electrode structure, the inset shows a magnified view of the region labeled in red rectangle. 2D map and EELS spectra of the core edges of O *K*, Mn *L*, and Ni *L* by EELS line scan from (c) fragmented piece and (d) cycled bulk; EELS line scan region is indicated by the green line in the inset Z-contrast image in panel c and d. (e) Detailed comparison of the O-*K*, Mn-*L*, and Ni-*L* edges of the fragmented piece, cycled bulk, and pristine material; the EELS spectra of fragmented piece was obtained from the region indicated with the red dot shown in panel (b); EELS spectra are normalized to the middle peak of the oxygen *K* edge for easy comparison; the inset in e shows the magnified 2D map comparison of the O *K* edge and Mn *L* edge from the EELS line scans acquired in the fragmented piece and cycled bulk.

representatively shown in Figure 4c, we noticed that some pieces with relatively smaller sizes exist in the cycled sample. Structurally, these small pieces are very disordered. Li, C, O, Mn, and Ni EELS maps were collected from the selected region of fragmented pieces. The C map shows that the fragmented pieces are mainly composed of carbon-containing solid electrolyte interphase. More detailed comparisons are summarized in Figure 4j–l, in which EELS spectra of the “cycled bulk” is acquired in the thin edge of the cycled bulk region as labeled by the blue dot (Figure 4c), while the “fragmented piece” spectra is acquired by summing up a few spectra in the EELS map as shown in Figure 4d–i. Both Mn-*L* and Ni-*L* are observable in the fragmented pieces (Figure 4j), which suggests that the fragmented pieces are separated from the bulk particles during repeated electrochemical activation, leaving the sponge-like surface in the cycled bulk crystal. For O *K* edges, the peak at the energy loss of  $\sim 528$  eV, indicated with arrows in Figure 4j, is associated with the transition of the O-1s core state to the

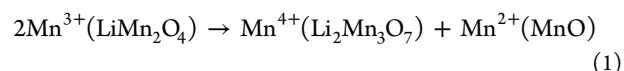
unoccupied O-2p states that are hybridized with TM-3d states.<sup>8</sup> The intensity of this peak can reflect the local vacant 3d states of the TM ions. Therefore, the valence states of TM ions can be compared based on this peak change. This peak drops drastically (almost disappears) in the fragmented pieces compared to a clear feature in the cycled bulk, demonstrating that the valence of the TM ions drops significantly in the fragmented pieces. This is consistent with the fine structure changes of the TM *L* edges as shown in Figure 4k. The Mn *L* edges are normalized to the  $L_3$  peak for easy comparison. There is a clear chemical shift of 2.25 eV toward the lower energy in the fragmented piece compared to the cycled bulk. In addition, the  $L_3/L_2$  ratio increases significantly in the fragmented piece compared to the cycled bulk. All of the fine structural signatures clearly show Mn ions have a much lower valence in the fragmented piece compared to the cycled bulk. A quantitative determination of the Mn valence based on the  $L_3/L_2$  ratio shows that the valence of Mn ion are 2+ in the fragmented pieces in comparison with 4+ in the cycled bulk region.<sup>8,20</sup> The

gigantic decrease in Mn valence will directly affect the stored Li content in the fragmented pieces, which is further supported by the much weaker Li K edge peak intensity in the fragmented particle than in the cycled bulk region (Figure 4l), suggesting that there is very limited Li content in the fragmented pieces.

To obtain further insight into the reason for capacity fading, the microstructure of another region indicated by green rectangle in Figure 4c is further investigated. The overall view of the bright field image is presented in Figure 5a, which shows that the layered structure of the pristine material has been destroyed and replaced with polycrystalline and amorphous regions distributed throughout the particle. The image was further magnified as shown in Figure 5b. In the inset of Figure 5b, the atomic scale Z-contrast image of the seemingly maintained fringe contrast region of this fragmented piece still shows obviously defected crystallinity, which is amorphized by repeated Li insertion/deinsertion. In contrast with the well-defined Li/O/TM layer that repeats in pristine material (Figure 2c), the TM layers and Li layers show comparable intensity, indicating that the TM ions migrated to the Li layers. This feature has been recognized as the transformation from layered structure to spinel.<sup>8,9</sup> In the present study, the electrode was charged/discharged for 300 cycles. The spinel phase formation has extended from the surface layer to the interior of the particles.<sup>9</sup> The progressive formation of spinel phase is consistent with the continuous discharge-voltage profile decay. Even worse, migration of TM ions to Li layers blocks the lithium ion diffusion channel and lithium sites, leading to capacity degradation and intrinsically low rate capability. At the same time, as shown clearly by Figure 5c–e, the prepeak of the O K edge from the fragmented piece shows negligible intensity, indicating a drop in the valence state of the Mn ions compared to the cycled bulk.<sup>21–25</sup> In addition, as shown by the 2D map of the line scan, the prepeak of the O K edge shows negligible intensity, and the Mn  $L_2$  peak drops significantly in intensity in all spots of the line scan across the fragmented piece compared to the cycled bulk region (inset in Figure 5e). All of these electronic signatures again disclose a valence state drop of the Mn ions in the fragmented piece after cycling.<sup>21–24</sup> The above results on the Mn valence state consistently mirror the EELS results in Figure 4, indicating the presence of  $Mn^{2+}$  in this region. To quantitatively compare the oxygen loss after cycling, we monitored the EELS core edge signal ratios between the transition metal ions and oxygen ions (e.g., Mn/O ratio = (Mn  $L$  edge signal integral)/(O K edge integral) after background subtraction using power law. The signal ratio of Ni/O and Mn/O is provided in Table S1 (Supporting Information). As shown clearly in the Table S1, the Mn/O signal ratio of the fragmented piece increased to  $\sim 0.803$  (compared to 0.422 of the pristine material) due to the release of oxygen species during the electrochemical cycling processes. The formation of oxygen vacancies is also consistent with the Mn valence drop as shown by the EELS fine structure analysis in Figures 4 and 5c–e. In addition, the Ni/O and Mn/O show similar values at the cycled bulk compared to the pristine state. Furthermore, comparing the Mn  $L$  edges of the pristine and the cycled bulk nanoparticles in Figure 5e, the Mn ions both show a 4+ valence in the cycled bulk and pristine nanoparticles. On the other hand, the Ni  $L$  edges shifted to a little higher energy loss value in the cycled bulk compared to the pristine nanoparticles, indicating a likely valence increase of Ni after cycling. This may be related to the fact that Ni ions migrate into the Li layers during cycling. In addition, the oxygen coordination environment for the Ni ions in Li layers is different from the pristine material due to the  $Li^+$  ion removal and associated oxygen ions reconfigura-

tion. The Li K edge shown in Figure S3 (Supporting Information) further substantiates that a very limited amount of Li is present in the fragmented piece even after final lithiation.

As discussed above, one possible reason for the formation of  $Mn^{2+}$  ions in the fragmented pieces is ascribed to the continuous extraction of oxygen from the surface structural lattice leads to formation of an oxygen deficient structure,  $Li_{1-x}MO_{2-\delta}$ , which lowers the oxidation valence of Mn for charge neutrality. The other more likely reason is that the spinel phase transformed from the original layered structure is not stable during cycling and further transforms to other stable manganese oxides, for example,  $Li_2Mn_3O_7$  and the like, via the loss of MnO, due to a disproportionate reaction of  $Mn^{3+}$ . As consistently supported by the results reported by Xia et al.,<sup>26</sup> the possible disproportionate reaction of  $Mn^{3+}$  could be described as follows:



It should be noted that the true reactions may be much more complicated due to the complex spinel phase structure and the existence of Ni ions in the electrode. Accompanying the loss of MnO, loss of NiO also occurs as evidenced by the presence of Ni peak in the fragmented pieces shown in Figure 4j. The loss of MnO and NiO results in the significant capacity loss of the  $Li[Li_{0.2}Ni_{0.2}Mn_{0.6}]O_2$  electrode. It is believed that the formation of spinel phase and the subsequent fragmentation and deactivation of TM ions are the dominant reasons for the continuous capacity fading during cycling.

The above result is understandable because the particle surface directly contacts the electrolyte and it is easy for it to be etched by the acidic species from the electrolyte. In addition to the trace HF in the electrolyte, the oxidation of carbonate solvents at high voltages  $>4.5$  V would also increase the formation of acidic species in the electrolyte.<sup>27</sup> The attack by acidic species would accelerate the disproportion of  $Mn^{3+}$ ,<sup>28</sup> which leads to the breakdown of the spinel-type phase. The etching of the cathode surface by the acidic species also produces the spongy surfaces of the cathode after cycling and the debris dispersed in the solid electrolyte interphase,<sup>28</sup> which explains the corrosion and fragmentation of the layered cathode material during cycling. The further degradation of the cathode crystal structure and formation of  $Mn^{2+}$  species result in significant capacity fading during long-term cycling. Surface coatings with  $Al_2O_3$ ,<sup>29</sup>  $AlF_3$ ,<sup>11</sup>  $Li_xMn_{1-x}O_2$ ,<sup>30</sup>  $Li-Ni-PO_4$ ,<sup>31</sup> and so forth have been repeatedly attested to be a facile and useful approach to improve the electrochemical performance of  $Li[Li_{0.2}Ni_{0.2}Mn_{0.6}]O_2$  or similar cathodes with  $Li_2MO_3$  character. The fundamental finding of this work could also reveal the functional mechanism of surface coatings. For example, the  $AlF_3$  coating could significantly improve the electrochemical performance of layered-structure materials,<sup>11,32</sup> although it could not stop the layered/spinel transformation.<sup>9</sup> We believe that the main function of surface coating is maintaining the structural stability/integrity of the cathode materials, prohibiting the etching by acidic species and suppressing the side reactions between the electrode and the electrolyte.

In summary, pristine and cycled layered-structure  $Li[Li_{0.2}Ni_{0.2}Mn_{0.6}]O_2$  samples have been characterized in detail by STEM combined with EELS to get insights about the origin of capacity fading. Due to cathode surface etching by acidic species, a sponge-like surface forms, and the etched pieces disperse in the solid electrolyte interphase after cycling. The crystallinity of the fragmented pieces is poor compared with the cycled bulk crystal

region. Furthermore, EELS fine structure analysis shows that the fragmented pieces retain a  $\text{Mn}^{2+}$  valence state, which significantly reduces the amount of lithium ions that can be stored in the cathode. This valence drop is likely to be the primary factor contributing to the continuous capacity loss. These results also shine light on the role of surface coating, for example,  $\text{AlF}_3$  coating, in improving the stability of layered cathode materials as reported by earlier literature articles. The main function of these coatings is to protect the electrode from etching by acidic species from the electrolyte, to suppress degradation of the cathode structure, and thus to improve the long-term cycling stability of the cathode.

## ■ ASSOCIATED CONTENT

### ■ Supporting Information

Experimental details for the material preparation, STEM and EELS characterization, along with the additional supporting data. This material is available free of charge via the Internet at <http://pubs.acs.org>.

## ■ AUTHOR INFORMATION

### Corresponding Author

\*C.W.: Tel. 509-371-6268; fax 509-371-6242; e-mail: [chongmin.wang@pnnl.gov](mailto:chongmin.wang@pnnl.gov). J.-G.Z.: Tel. (509)-372-6515; fax 509-375-2186; e-mail: [jiguang.zhang@pnnl.gov](mailto:jiguang.zhang@pnnl.gov).

### Author Contributions

J.Z. and M.G. contributed equally to this work.

### Notes

The authors declare no competing financial interest.

## ■ ACKNOWLEDGMENTS

This work is supported by the Assistant Secretary for Energy Efficiency and Renewable Energy, Office of Vehicle Technologies of the U.S. Department of Energy under Contract No. DE-AC02-05CH11231, Subcontract No. 18769, under the Batteries for Advanced Transportation Technologies program. The microscopic study described in this paper is part of the Chemical Imaging Initiative at Pacific Northwest National Laboratory (PNNL). It was conducted under the Laboratory Directed Research and Development Program at PNNL, a multiprogram national laboratory operated by Battelle for the U.S. Department of Energy (DOE). The work was conducted in the William R. Wiley Environmental Molecular Sciences Laboratory (EMSL), a national scientific user facility sponsored by DOE's Office of Biological and Environmental Research and located at PNNL. PNNL is operated by Battelle for the DOE under Contract DE-AC05-76RLO1830.

## ■ REFERENCES

- (1) Thackeray, M. M.; Johnson, C. S.; Vaughey, J. T.; Li, N.; Hackney, S. A. *J. Mater. Chem.* **2005**, *15*, 2257.
- (2) Thackeray, M. M.; Kang, S.-H.; Johnson, C. S.; Vaughey, J. T.; Benedek, R.; Hackney, S. A. *J. Mater. Chem.* **2007**, *17*, 3112.
- (3) Johnson, C. S.; Kim, J. S.; Lefief, C.; Li, N.; Vaughey, J. T.; Thackeray, M. M. *Electrochem. Commun.* **2004**, *6*, 1085.
- (4) Johnson, C. S.; Li, N.; Lefief, C.; Thackeray, M. M. *Electrochem. Commun.* **2007**, *9*, 787.
- (5) Yu, H.; Zhou, H. *J. Phys. Chem. Lett.* **2013**, *4*, 1268.
- (6) Johnson, C. S.; Li, N.; Lefief, C.; Vaughey, J. T.; Thackeray, M. M. *Chem. Mater.* **2008**, *20*, 6095.
- (7) Ito, A.; Shoda, K.; Sato, Y.; Hatano, M.; Horie, H.; Ohsawa, Y. *J. Power Sources* **2011**, *196*, 4785.

- (8) Xu, B.; Fell, C. R.; Chi, M.; Meng, Y. S. *Energy Environ. Sci.* **2011**, *4*, 2223.
- (9) Gu, M.; Belharouak, I.; Zheng, J.; Wu, H.; Xiao, J.; Genc, A.; Amine, K.; Thevuthasan, S.; Baer, D. R.; Zhang, J.-G.; Browning, N. D.; Liu, J.; Wang, C. *ACS Nano* **2012**, *7*, 760.
- (10) Yu, H.; Wang, Y.; Asakura, D.; Hosono, E.; Zhang, T.; Zhou, H. *RSC Adv.* **2012**, *2*, 8797.
- (11) Zheng, J. M.; Zhang, Z. R.; Wu, X. B.; Dong, Z. X.; Zhu, Z.; Yang, Y. *J. Electrochem. Soc.* **2008**, *155*, A775.
- (12) Zheng, J. M.; Wu, X. B.; Yang, Y. *Electrochim. Acta* **2011**, *56*, 3071.
- (13) Zheng, J.; Zhu, D.; Yang, Y.; Fung, Y. *Electrochim. Acta* **2012**, *59*, 14.
- (14) Lu, Z.; Dahn, J. R. *J. Electrochem. Soc.* **2002**, *149*, A815–A822.
- (15) Armstrong, A. R.; Holzapfel, M.; Novák, P.; Johnson, C. S.; Kang, S.-H.; Thackeray, M. M.; Bruce, P. G. *J. Am. Chem. Soc.* **2006**, *128*, 8694.
- (16) Gu, M.; Belharouak, I.; Genc, A.; Wang, Z.; Wang, D.; Amine, K.; Gao, F.; Zhou, G.; Thevuthasan, S.; Baer, D. R.; Zhang, J.-G.; Browning, N. D.; Liu, J.; Wang, C. *Nano Lett.* **2012**, *12*, 5186.
- (17) Ito, A.; Li, D.; Sato, Y.; Arao, M.; Watanabe, M.; Hatano, M.; Horie, H.; Ohsawa, Y. *J. Power Sources* **2010**, *195*, 567.
- (18) Lei, C. H.; Bareño, J.; Wen, J. G.; Petrov, I.; Kang, S. H.; Abraham, D. P. *J. Power Sources* **2008**, *178*, 422.
- (19) Miller, D. J.; Proff, C.; Wen, J. G.; Abraham, D. P.; Bareño, J. *Adv. Energy Mater.* **2013**, DOI: 10.1002/aenm.201300015.
- (20) Wang, Z. L.; Yin, J. S.; Jiang, Y. D. *Micron* **2000**, *31*, 571–580.
- (21) Yang, F.; Gu, M.; Arenholz, E.; Browning, N. D.; Takamura, Y. *J. Appl. Phys.* **2012**, *111*, 013911.
- (22) He, C.; Grutter, A. J.; Gu, M.; Browning, N. D.; Takamura, Y.; Kirby, B. J.; Borchers, J. A.; Kim, J. W.; Fitzsimmons, M. R.; Zhai, X.; Mehta, V. V.; Wong, F. J.; Suzuki, Y. *Phys. Rev. Lett.* **2012**, *109*, 197202.
- (23) Gu, M.; Song, C.; Yang, F.; Arenholz, E.; Browning, N. D.; Takamura, Y. *J. Appl. Phys.* **2012**, *111*, 084906.
- (24) Gu, M.; Genc, A.; Belharouak, I.; Wang, D.; Amine, K.; Thevuthasan, S.; Baer, D. R.; Zhang, J.-G.; Browning, N. D.; Liu, J.; Wang, C. *Chem. Mater.* **2013**, *25*, 2319.
- (25) Gu, M.; Dearden, C. R.; Song, C.; Browning, N. D.; Takamura, Y. *Appl. Phys. Lett.* **2011**, *99*, 261907.
- (26) Xia, Y.; Zhou, Y.; Yoshio, M. *J. Electrochem. Soc.* **1997**, *144*, 2593–2600.
- (27) Robertson, A. D.; Bruce, P. G. *Chem. Mater.* **2003**, *15*, 1984.
- (28) Jang, D. H.; Shin, Y. J.; Oh, S. M. *J. Electrochem. Soc.* **1996**, *143*, 2204–2211.
- (29) Wu, Y.; Manthiram, A. *Electrochem. Solid-State Lett.* **2006**, *9*, A221.
- (30) Zhao, Y.; Zhao, C.; Feng, H.; Sun, Z.; Xia, D. *Electrochem. Solid-State Lett.* **2011**, *14*, A1.
- (31) Kang, S.-H.; Thackeray, M. M. *Electrochem. Commun.* **2009**, *11*, 748.
- (32) Sun, Y.-K.; Lee, M.-J.; Yoon, C. S.; Hassoun, J.; Amine, K.; Scrosati, B. *Adv. Mater.* **2012**, *24*, 1192.